Economic Geology, v. XXX, no. XX, pp. X–X

Zircon and Whole-Rock Trace-Element Indicators of Magmatic Hydration State and Oxidation State Discriminate Copper Ore-Forming from Barren Arc Magmas

Robert R. Loucks,† Gonzalo J. Henríquez, and Marco L. Fiorentini

Centre for Exploration Targeting, School of Earth Sciences, University of Western Australia, 35 Stirling Highway, Crawley, Perth, Western Australia 6009

Abstract

To meet surging requirements of copper for the green energy revolution, minable resources subequal to all copper production in history must be found in the next two decades. We show that trace elements in zircon and whole-rock samples that are diagnostic of unusually high-pressure magmatic differentiation and high hydration state and oxidation state of their parent silicate melt are effective for discriminating copper sulfide-ore-productive arc magmas from infertile arc magmas. Tests on our database of 5,777 zircons from 80 igneous complexes, including 2,220 zircons from ore-generative intrusions in 37 major porphyry and high-sulfidation epithermal Cu(-Au-Mo) deposits worldwide, demonstrate that our magmatic copper-fertility discriminants apparently perform equally well in intraoceanic arcs, continental margin arcs, and continental collision orogens of Ordovician to Quaternary age. That performance consistency means that the tectono-magmatic controls on development of magmatic-hydrothermal copper ore-forming fertility are essentially the same in all those plate-convergence settings. The ratio $Ce/\sqrt{(U \times Ti)}$ in zircon is a quantitative indicator of the relative oxygen fugacity of the silicate melt and its sulfur-carrying capacity. The ratio of the europium anomaly to ytterbium in granitoid melts and zircon is an uncalibrated but empirically useful indicator of the melt's hydration state and ability to provide chloride-complexed metals to exsolving hydrothermal fluids. Plots of $(Eu_N/Eu^*)/Yb_N$ vs. $Ce/\sqrt{(U \times Ti)}$ in zircon are remarkably effective for discriminating igneous complexes, arc segments, and time intervals within them that can generate and are likely to host magmatic-hydrothermal Cu(-Au-Mo) ore deposits. Arrays of cognate zircons on such plots have slopes that vary with pressure-dependent chlorinity of exsolving fluid and its efficacy in scavenging CuCl from the melt. Our zircon indicators of Cu metallogenic fertility are applicable to detrital as well as in situ zircons and can assist with ore discovery in watersheds upstream from a sediment sampling site. We formulated a composite zircon copper fertility index (ZCFI) that can be applied to each microbeam spot analysis—$ZCFI = 10^4 (Eu_N/Eu_N^*)/Yb_N + 5\ Ce/\sqrt{(U_i \times Ti)}$—and substantially decreases the number of zircon analyses needed for reliable prospectivity assessment in a detrital grain population, thereby making this watershed-scale exploration tool cost-competitive with other methods of geochemical exploration.

Introduction

The world's annual copper needs are projected to be 35 million tonnes (Mt) by 2040, in part because of the drive toward low-carbon energy sources and a lower-carbon-emissions world (Arndt et al., 2017; International Energy Agency, 2021). To meet the requirements of wind turbines, electric vehicles, and other green technologies, production subequal to all copper production in history (~640 Mt) must be found in the next two decades. Discovery of new magmatic-hydrothermal copper sulfide ore deposits can be enhanced by identifying differences in the chemical compositions of copper ore-forming granitoid magmas and accessory minerals such as zircon, as compared to whole-rock and zircon compositions of ordinary, barren granitoid rocks.

Arc magmas parental to porphyry copper deposits (PCDs) are not distinguished from ordinary calc-alkalic arc magmas by unusual Cu contents (Audétat and Pettke, 2006; Zhang and Audétat, 2017; Du and Audétat, 2020; Grondahl and Zajacz, 2022). Instead, they are distinguished by high values of lithophile element ratios that represent unusually high oxidation and hydration states of parental silicate melts (Rohrlach and Loucks, 2005; Loucks, 2014, 2021; Loucks et al., 2020). The melt oxidation state strongly influences the sulfur content of granitoid melts and exsolving hydrothermal fluids (Zajacz et al., 2012; Fortin et al., 2015; Matjuschkin et al., 2016; Xu et al., 2022). The melt hydration state coordinates variations in depth of fluid exsolution, fluid/melt partition coefficients, and concentrations of CuCl and other chloride salts in exsolving hydrothermal fluids (Botcharnikov et al., 2015; Tattitch and Blundy, 2017; Hsu et al., 2019; Tattitch et al., 2021; Loucks and Fiorentini, 2023b, and references therein).

We provide new evidence for unusually high hydration and oxidation states of PCD-forming silicate melts, as recorded by trace elements in zircon, which is mechanically and chemically robust enough to make detrital zircons useful as guides to watersheds containing Cu-fertile igneous complexes upstream from the sediment sampling site. We describe a case study illustrating the utility of detrital zircons for porphyry Cu(-Au-Mo) exploration.

Magmatic Differentiation Trends in Orogenic and Nonorogenic Arc Segments Compared

Lateral variations of tectonic stress along convergent plate margins have profound effects on the chemical course of magmatic differentiation of mantle-derived basaltic magmas. The U-Pb age range in single zircon crystals and in cognate zircon suites from PCD-related intrusions commonly indicates a multimillion-year lifespan of the parental magma (e.g., Valencia et al., 2005; Nathwani et al., 2021). This lifespan greatly exceeds crystallization timespans of upper-crustal plutons and implies slow cooling during long storage in a deep (Moho-vicinity) magma chamber in a horizontally compressive stress

†Corresponding author: email, robert.loucks@uwa.edu.au

ISSN 0361-0128; doi:10.5382/econgeo.5071; 13 p.
Digital appendices are available in the online Supplements section.

Submitted: March 24, 2023/Accepted: November 29, 2023

regime that inhibits the ascent of buoyant magma by dike propagation (Loucks, 2021, and references therein).

As horizontal compressive stress increases during orogeny, resistance to magma ascent by buoyancy-driven dike propagation increases, so more advanced chemical differentiation is achieved at deeper crustal levels (Loucks, 2021). The typical temperature of fluid-undersaturated country rock at the arc Moho (~750° ± 50°C) is higher than the magma's wet solidus temperature (~640°C), so residual felsic melts in such Moho-vicinity stress traps cannot freeze by conductive heat loss to country rocks and are likely to last long enough to experience intermittent replenishments by hydrous basaltic melts (Loucks, 2021). In a Moho-vicinity chamber, replenishing mantle melts mix with resident residual melts, and over a succession of replenishment and crystallization cycles, hybrid melts inherit an accumulation of chemical components that were largely excluded from cumulus minerals (H_2O, Cl, SO_3, CO_2, Sr, Eu^{2+}, Fe^{3+}; O'Hara and Matthews, 1981).

High H_2O, Cl, and SO_3 contents of residual granitoid melts having ordinary Cu contents endow them with copper ore-forming fertility when such melts escape toward the surface as orogenic stress resistance to dike propagation wanes near the end of orogeny. Periods and locales of stress relaxation in contractional tectonic settings have been recognized for decades as empirically favorable for the generation of porphyry and high-sulfidation epithermal Cu(-Au-Mo) ore deposits (see literature review by Sillitoe, 2010).

Figure 1 compares P_{H_2O}-sensitive (where P = pressure) lithophile element ratios in whole-rock analyses from barren arc segments to ratios of the same elements in least altered samples from igneous complexes that host major high-sulfidation epithermal and porphyry Cu(-Au-Mo) ore deposits in intraoceanic and continental margin magmatic arcs. The Sr/Y and $(Eu_N/Eu^*)/Yb_N$ ratios in silicate melts primarily reflect the relative proportions of hornblende and plagioclase that have segregated from the melt during magmatic differentiation to the stage sampled. Magmatic differentiation at high P_{H_2O} delays plagioclase saturation in the paragenetic sequence of igneous minerals and suppresses the cumulative modal proportion of plagioclase, which is a sink for Eu^{2+} and Sr^{2+}, thereby allowing Eu^{2+} and Sr^{2+} to accumulate in residual melt until it eventually attains plagioclase saturation (Loucks, 2014, 2021). Magmatic differentiation at high P_{H_2O} induces early and prolific production of hornblende, which is a sink for Y, Yb, and Sc, imposing depletion of those elements in the melt as differentiation progresses (Naney, 1983; Moore and Carmichael, 1998; Loucks, 2021, and table 2 therein; Tatnell et al., 2023). Consequently, to the degree that high-pressure and high dissolved H_2O promote early and prolific hornblende production and delayed and diminished plagioclase production, magmas in Moho-vicinity stress traps evolve to residual andesitic and dacitic melts having adakitic high Sr/Y and Eu/Yb ratios (Rohrlach and Loucks, 2005; Macpherson et al., 2006; Loucks, 2014 and 2021; Nandedkar et al., 2016; Tatnell et al., 2023; Loucks and Fiorentini, 2023b). The strong correlation of whole-rock $(Eu_N/Eu^*)/Yb_N$ with redox-independent Sr/Y (Fig. 1; App. Table A1) means that they have the same mineralogic controls and essentially the same sensitivity to hydration state and insensitivity to oxidation state of the silicate melt during magmatic differentiation.

Hornblende is a much more significant host of Fe^{3+} than augite and hypersthene (King et al., 2000; Goltz et al., 2022), so early and prolific hornblende production at high P_{H_2O} delays and diminishes production of titanomagnetite, which is a major sink for V^{3+} and V^{4+}, thereby allowing the residual melt to retain more V to advanced stages of magmatic differentiation at high P_{H_2O}, while hornblende-dominated differentiation depletes the melt of Sc, permitting the V/Sc ratio to rise in residual melts (red arrays in Fig. 1; see also modeling by Loucks, 2021, and table 2 therein). In contrast, magmatic differentiation dominated by pyroxenes + plagioclase + titanomagnetite at low P_{H_2O} (blue arrays in Fig. 1) induces strong depletion of Sr, Eu, and V and avoids depletion of Y and heavy rare earth elements (REEs) from residual melts. In titanomagnetite-saturated granitoid melts, the partition coefficient $D_V^{mag/melt}$ decreases strongly with increasing oxidation state of the melt, permitting retention of more V in more oxidized residual melts (Arató and Audétat, 2017).

Copper ore-productive and nonmineralizing magmatic differentiation trends in Figure 1 diverge from the same type of basaltic parent magma according to the difference of the ambient stress field in laterally adjacent arc segments above the same subduction zone. This demonstrates that Cu metallogenic fertility is an emergent property of the magmatic differentiation process, not a primary property of the parental mafic melt. Atypical melting conditions, chemically unusual melt source regions, or assimilation of components from country rock are not implicated as common causes of magmatic copper fertility. The main controls are horizontal stress, the depth of the most magmatic differentiation, and the number of replenishment-crystallization cycles, which tend to be geodynamically coordinated.

Zircon $(Eu_N/Eu^*)/Yb_N$ is an Indicator of Melt Hydration State

Figure 2 shows that zircon inherits from its parent melt the REE characteristics diagnostic of Cu metallogenic fertility and infertility. Figure 2b shows that zircon inherits the strong Eu depletion typical of Cu-infertile parental granitoid melts that evolved at relatively low P_{H_2O} by segregation of pyroxenes and plagioclase. Copper ore-forming granitoid melts typically have a minimum in their REE patterns in the Dy-Er interval (Fig. 2c) owing to selective removal of those REEs by early and prolific cumulus hornblende. Ore-forming melts typically have $Eu_N/Eu^* \geq 1$ (Fig. 2c; App. Table A1), but zircons in Cu ore-forming granitoid intrusions display slight dips at Eu (Fig. 2d). Lattice strain inhibits substitution of the large Eu^{2+} ion (1.25 Å) relative to the smaller Eu^{3+} ion (1.066 Å) in Zr^{4+} (0.84 Å) lattice sites (ionic radii from Shannon, 1976), whereas the melt is nondiscriminatory, so magmatic zircon always has lower Eu^{2+}/Eu^{3+} and Eu_N/Eu^* ratios than its parent melt. Owing to thermal contraction of the zircon crystal lattice, the difference of Eu_N/Eu^* between melt and zircon increases with decreasing crystallization temperature (Loucks et al., 2018).

Zircon $Ce/\sqrt{(U \times Ti)}$ Measures Magmatic Oxidation State

Melts having higher contents of dissolved H_2O crystallize at lower temperatures than anhydrous compositional analogues (Naney, 1983; Moore and Carmichael 1998). Temperature-

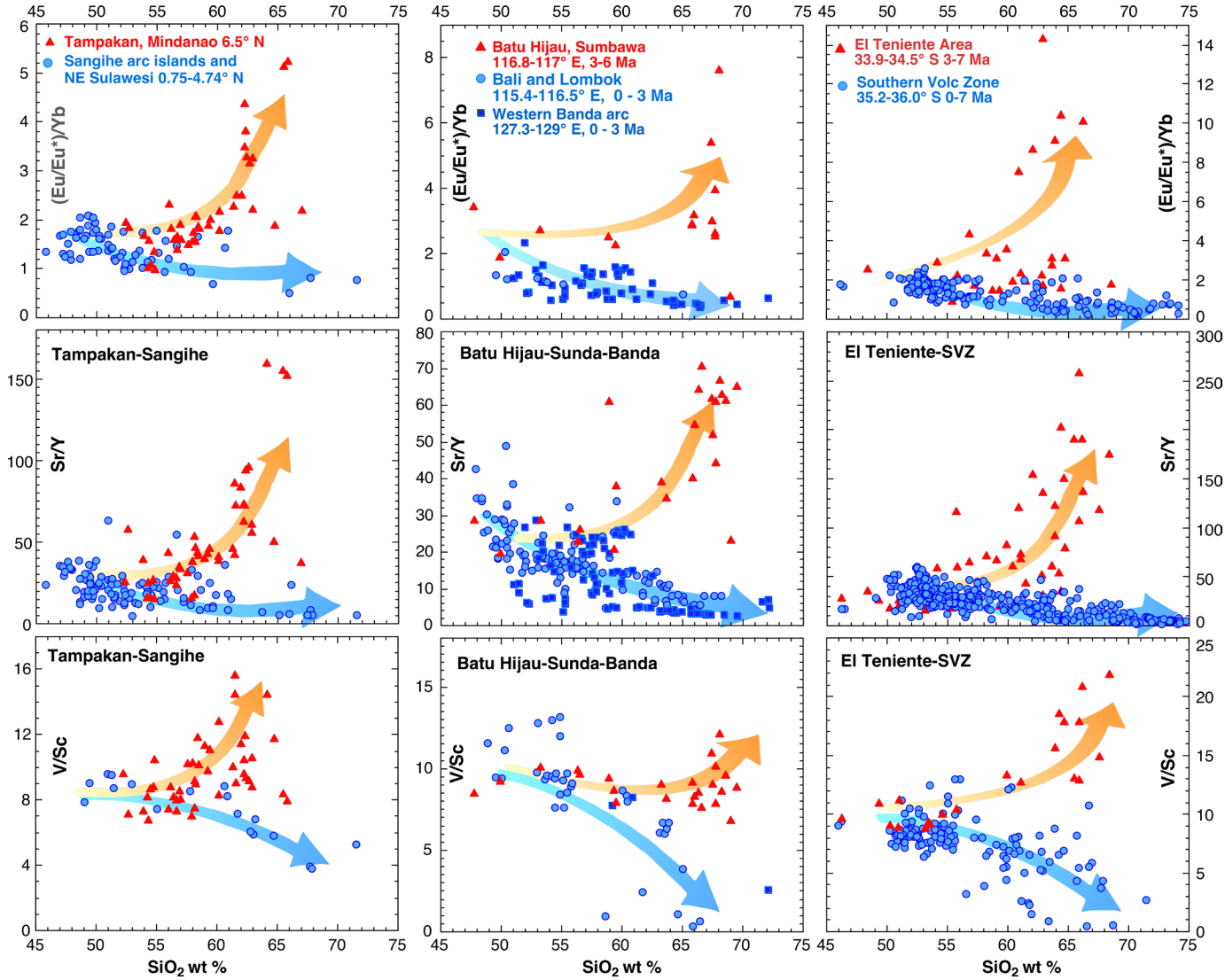

Fig. 1. Comparison of whole-rock, lithophile element proxies for hydration state of mafic-to-felsic magmatic differentiation series in orogenically deforming, ore-bearing arc segments (red) and penecontemporaneous, laterally adjacent, nonorogenic, ore-deficient arc segments (blue) above the same subduction zone. Differentiation trends (increasing wt % SiO_2) diverge from the same type of arc-basaltic parent magma according to the stress regime, which controls the depth at which most mafic-to-felsic magmatic differentiation occurs, and in turn, strongly influences the melt's dissolved H_2O content and the paragenetic sequence and modal proportions of crystallizing minerals and, hence, the trace element evolution of residual melts (Loucks, 2014; 2021). More analyses report Sr and Y than report V, Sc, and rare earth elements (REEs). In the left column of panels, red symbols represent variation of the ratios $(Eu_N/Eu^*)/Yb_N$ (normal mid-ocean-ridge basalt-normalized REEs), Sr/Y, and V/Sc in all available whole-rock analyses of samples retaining fresh or little-altered igneous plagioclase and hornblende and spanning a range of wt % SiO_2 representing the mafic-to-felsic differentiation series in the 7 to 1 Ma igneous complex. The complex hosts the giant Tampakan porphyry and high-sulfidation Cu-Au deposits of Pliocene age, south-central Mindanao, Philippines, at the orogenically deforming north end of the Sangihe intraoceanic island arc above the subducting Molucca Sea plate (Rohrlach and Loucks, 2005). Blue dots represent the mafic-to-felsic differentiation series in Pliocene and Quaternary igneous suites in a nonorogenic interval of the Sangihe arc southward from Mindanao to the northeastern tip of Sulawesi, wherein no significant copper mineralization has been reported. In the center column of panels, red triangles represent whole-rock analyses of least-altered samples in the late Neogene mafic-to-felsic differentiation series in the igneous complex hosting the Batu Hijau porphyry Cu-Au deposit in an orogenic stress setting on Sumbawa Island, Indonesia (Fiorentini and Garwin, 2010). Blue symbols represent the differentiation series in relatively noncompressive intervals above the same Sunda-Banda subduction zone farther east along the western Banda arc (Romang, Damar, Teon, and Nila volcanic islands, blue dots), and west of Sumbawa in Lombok and Bali (Rinjani, Batur, Agung, and Seraja magmatic centers, blue squares). In the right column of panels, red symbols represent all available whole-rock analyses of samples retaining fresh or little-altered igneous plagioclase in the mafic-to-felsic differentiation series in the area encompassing the giant El Teniente porphyry Cu(-Mo-Au) ore deposit at the south end of the Neogene Sierras Pampeanas fold-and-thrust belt in the central Andes (Stern et al., 2011). The plotted age range (7–3 Ma) includes pre-ore stages of magmatic differentiation leading to ore-stage magmas having 65 to 70 wt % SiO_2 (anhydrous basis). Blue symbols represent all available whole-rock analyses in the 7 to 0 Ma age range in a well explored, relatively noncompressive arc interval lacking economically significant mineralization a short distance south of El Teniente above the same subducting Nazca Plate. Appendix Table A1 lists the plotted analyses and literature sources.

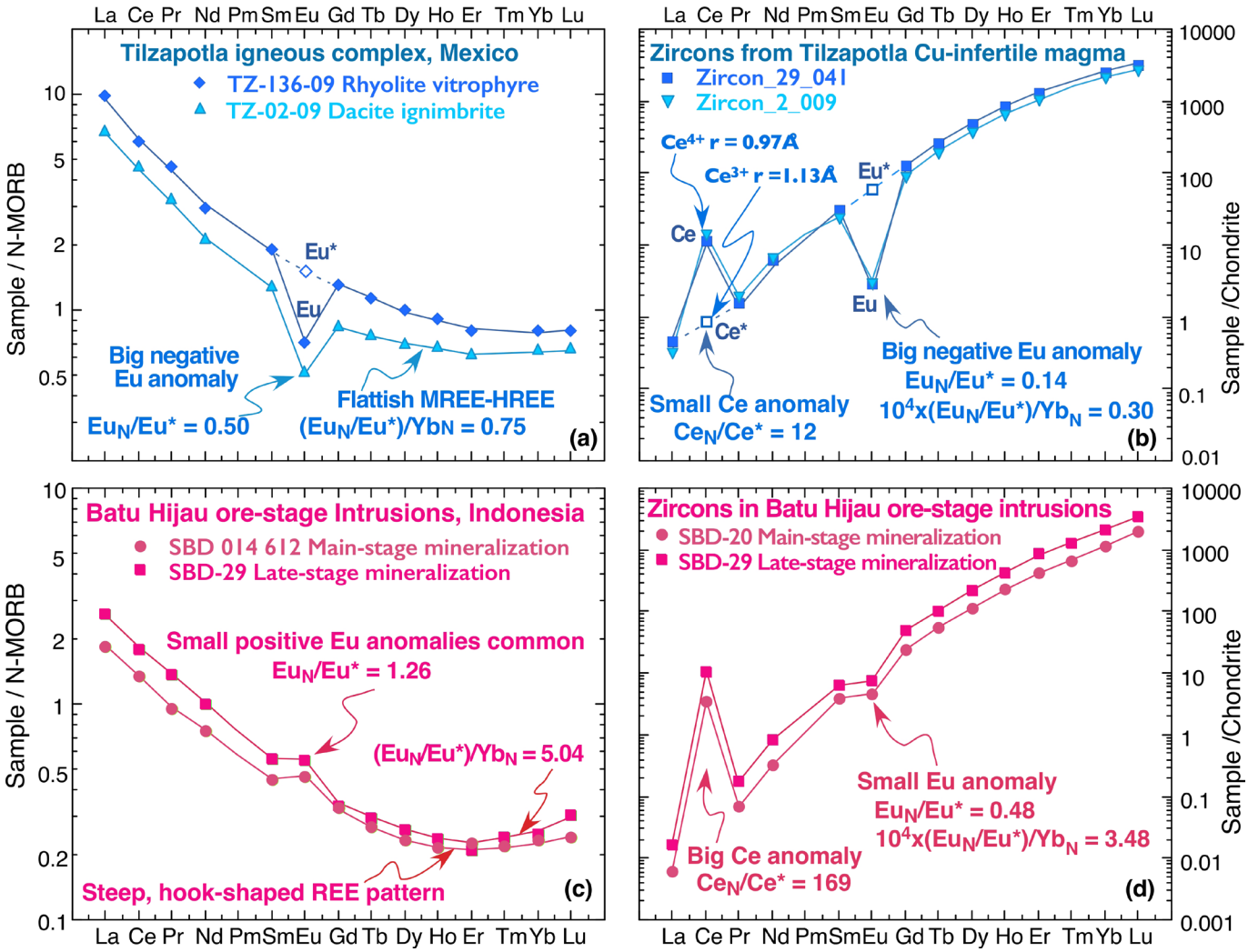

Fig. 2. Distinctions between copper ore-forming and infertile whole-rock and zircon compositions. (a) Whole-rock rare earth elements (REEs, normalized to normal mid-ocean-ridge basalt) of 34 to 32 Ma units in the Tilzapotla caldera, Guerrero, Mexico (Mori et al., 2012) illustrate features typical of Cu-infertile, H_2O-poor calc-alkalic granitoid arc magmas that evolved mainly by segregation of cumulus pyroxenes and plagioclase: (1) a subhorizontal pattern in the mid- to heavy REE Tb-Yb interval, and (2) a pronounced negative Eu anomaly. These impart low values of $(Eu_N/Eu^*)/Yb_N \approx 0.75$ in these examples. The Eu anomaly in whole-rocks and zircons is the ratio of measured Eu_N-to-Eu^* where $Eu^* \equiv \sqrt{(Sm_N \times Gd_N)}$. (b) Chondrite-normalized REEs in representative zircons from the Tilzapotla ignimbrite reported by Martiny et al. (2013) have large Eu anomalies, low values of $(Eu_N/Eu^*)/Yb_N \approx 0.30$, and small Ce anomalies, Ce/Ce^*, where $Ce^*\sqrt{(La_N \times Pr_N)}$. (c) Steep, spoon-profile REE patterns with a minimum near Er and absence of a significant negative Eu anomaly are typical of porphyry-copper-productive, H_2O-rich granitoid arc magmas that have evolved at high pressure mainly by precipitating hornblende-rich, plagioclase-free cumulates, such as these examples in the Batu Hijau Cu-Au deposit, Sumbawa (Fiorentini and Garwin, 2010). These features produce a relatively large value of $(Eu_N/Eu^*)/Yb_N \approx 5.0$. (d) Zircon analyses by Lu et al. (2016) in ore-forming intrusions at Batu Hijau illustrate the low-amplitude Eu anomaly, much higher $(Eu_N/Eu^*)/Yb_N \approx 3.5$, and large-amplitude Ce spikes typical of zircons from H_2O-rich, low-temperature, porphyry-copper-forming magmas globally. Abbreviations: HREE = heavy rare earth element, MREE = mid-rare earth element.

sensitive lattice strain is selective for the smaller Ce^{4+} ion (0.97 Å) relative to Ce^{3+} (1.13 Å) in Zr^{4+} (0.84 Å) lattice sites, so the ratio of zircon/melt partition coefficients, $D^{zirc/melt}_{Ce^{4+}}/D^{zirc/melt}_{Ce^{3+}}$, increases by ~4 orders of magnitude over the cooling interval 1,300° to 700°C (Loucks et al., 2018). This effect contributes to the contrasting amplitudes of Ce spikes in Figure 2b, d. As described by Loucks et al. (2020, and references therein), attempts to calibrate and apply zircon Ce^{4+}/Ce^{3+} (or Ce/Ce^*) as an indicator of melt oxidation state have been frustrated by extreme sensitivity to temperature and to major element composition of the parent melt, including wt % H_2O dissolved in the melt during zircon crystallization.

Loucks et al. (2020) and Loucks and Fiorentini (2023b) thermodynamically derived the ratio $Ce/\sqrt{(U_i \times Ti)}$ in zircon as a precise measure of the melt oxidation state (independent of melt hydration state, temperature, and pressure) corresponding to ΔFMQ (i.e., $\log f^{sample}_{O_2} - \log f^{FMQ}_{O_2}$), wherein FMQ is the reference buffer fayalite + magnetite + quartz, and U_i is initial uranium content of the dated zircon calculated from measured parts per million U to account for radioactive decay

since crystallization. Loucks et al. (2020) empirically calibrated $Ce/\sqrt{(U_i \times Ti)}$ in zircon as a magmatic oxybarometer using 1,042 analyzed zircons in 85 natural populations having independently constrained log f_{O_2} in the range FMQ –4.9 to FMQ +2.9. The advantages of $Ce/\sqrt{(U_i \times Ti)}$ over previous attempts to formulate a Ce-in-zircon oxybarometer are: (1) it is more precise (standard error of 0.6 log unit f_{O_2} in metaluminous to mildly peraluminous and mildly peralkaline wet or dry melts in the composition range from kimberlite to rhyolite at 650° to 1,300°C, and from 0 to at least 40 kb), (2) it is easy to use, and (3) it is applicable to out-of-context detrital zircons because it is formulated to eliminate dependence on temperature, pressure, and major element composition of the melt, including dissolved wt % H_2O.

Granitoid melts parental to the El Salvador PCDs (Fig. 3), El Teniente, and many other major porphyry and high-sulfidation epithermal-type Cu-Au deposits were cosaturated in magmatic anhydrite and monosulfide solid solution (mss) (Hutchinson and Dilles, 2019, and references therein). Therefore, the sulfur concentration in hydrothermal fluid exsolving from such silicate melts at any given pressure and temperature is the sum of the aqueous solubility of anhydrite and aqueous solubility of mss, causing the fluid's total dissolved S to peak at log $f_{O_2} \approx$ FMQ + 1.5 at the sulfide-sulfate redox transition in the melt and in the phenocryst assemblage (Zajacz et al., 2012). Figure 3 and other zircon oxybarometry data presented here show that most PCD-forming magmas have log $f_{O_2} \approx$ FMQ + 1.5 ± 0.5 upon arrival at ore-forming depths. This is a useful constraint for recognition of watersheds containing Cu-fertile igneous complexes that are the source of detrital zircons.

Covariation of $(Eu_N/Eu^*)/Yb_N$ and ΔFMQ or $Ce/\sqrt{(U \times Ti)}$ in Melts and Zircons

During crystallization-differentiation of arc magmas in Moho-vicinity storage chambers at high P_{H_2O}, zircon tends to saturate before plagioclase at a mafic stage of magmatic differentiation (Loucks and Fiorentini, 2023a, b), and zircon's trace element variations can record much of the melt's compositional evolution, spanning a wide compositional range. Mid- and upper-crustal magmatic differentiation dominated by pyroxene + plagioclase + titanomagnetite segregation at low P_{H_2O} typically reaches zircon saturation at advanced stages of melt evolution (≳70 wt % SiO_2), in which case a shorter composition range of cognate zircons reflects only later stages of magmatic differentiation (Loucks and Fiorentini, 2023a).

Figure 3 compares trends of evolving melt hydration state and oxidation state as derived from independent hornblende and zircon indicators. During the late Eocene Incaic orogeny in the central Andes, magmas parental to the Turquoise Gulch PCD, El Salvador district, evolved to granitoid stages of magmatic differentiation at lower-crustal pressures (Fig. 3a, b), as is typical of PCD-forming arc magmas globally, as constrained by Al-in-hornblende geobarometry (fig. 7 in Loucks, 2021) and by experimentally constrained modeling of whole-rock REE patterns (Tatnell et al., 2023). During ascent toward ore-forming depths, the Turquoise Gulch granitoid melts began to exsolve hydrothermal fluid at lower-crustal depths in response to decompression, as recorded by compositions of hornblende phenocrysts in ore-related intrusions analyzed by Lee (2008). Al-in-hornblende geobarometry (experimentally calibrated by Mutch et al., 2016) and hornblende-based indicators of dissolved wt % H_2O and oxidation state (ΔFMQ) in decompressing melt (calibrated by Ridolfi et al., 2010, using compiled experiments) are concordant with our zircon-based indicators (Fig. 3c) of silicate melt hydration state and oxidation state as applied to zircon compositions reported by Lee et al. (2017) in the same intrusions.

The dissolved wt % H_2O indicated in Figure 3a corresponds to $P_{H_2O} < P_{total}$ that is represented by Al-in-hornblende barometry. It is likely that the apparent deficit of fluid pressure in these fluid saturated melts is largely accounted for by CO_2, for which we lack analyses in the plotted samples. At Moho-vicinity depths, fluid-undersaturated arc magmas typically contain a few thousand parts per million dissolved CO_2 that contributes several kilobars of P_{CO_2} to the total fluid pressure at the onset of fluid saturation (Blundy et al., 2010; Wallace et al., 2021) and brings the total fluid pressure into the range indicated by Al-in-hornblende barometry.

Figure 3c compares zircon compositions in representative Cu ore-productive and barren calc-alkalic granitoid intrusions in the central Andes. Our analyses of zircons in a late Neogene calc-alkalic granitoid intrusion in the Villalobos igneous complex at 36.2°S in Chile's southern volcanic zone (described by Sellés Mathieu, 2006; devoid of economically significant Cu mineralization) illustrate a typical contrast of magmatic differentiation trend between ore-forming and infertile suites. The contrast in slopes of the zircon arrays in Figure 3c (i.e., rate of melt oxidation per increment of H_2O loss) mainly reflects (1) the difference in the redox-modulated abundance of sulfate in the melt—which oxidizes Fe and Ce (and other elements) in residual melt—as fluid exsolves and gravitationally segregates (Scaillet et al., 1998); and (2) the depth at which fluid exsolution begins, which depends on the hydration state of the melt and strongly correlates with variation of the fluid/melt partition coefficient of $FeCl_2$ and the Fe^{2+}/Fe^{3+} ratio in exsolving hydrothermal fluid and residual melt. Compilations of experimental studies measuring the partition coefficient of Cl between hydrothermal fluid and andesitic to haplo-rhyolitic melts indicate ~10-fold decrease in $D_{Cl}^{fluid/melt}$ over the decompression interval 10 to 1 kbar (fig. 13 in Botcharnikov et al., 2015; fig. 5 in Hsu et al., 2019). The fluid/melt partition coefficient of Fe^{2+} as aqueous $FeCl_2$ is proportional to the square of the fluid's Cl concentration. Ferric chloride complexes are insignificant at redox conditions and Cl contents typical of exsolving magmatic hydrothermal fluids, whereas $FeCl_2$ typically is a major component of magmatic hydrothermal fluids exsolving from andesitic and dacitic melts (Bell and Simon, 2011; Zajacz et al., 2012). Granitoid melts richer in H_2O begin at higher pressure to exsolve and gravitationally segregate hydrothermal fluid having more $FeCl_2$ and higher Fe^{2+}/Fe^{3+}, which, in residual melt, tends to produce a higher rate of oxidation per increment of fluid loss and a shallower slope of zircon arrays in plots of $(Eu_N/Eu^*)/Yb_N$ vs. $Ce/\sqrt{(U_i \times Ti)}$. The fluid's efficiency of Cu extraction from the melt is also proportional to pressure-dependent chlorinity of exsolving fluid (Tattitch and Blundy, 2017; Tattitch et al., 2021). A shallower slope of a zircon array that crystallized from fluid-saturated melt is therefore expected to reflect a greater melt hydration state, greater depth of fluid saturation, greater aqueous sulfur

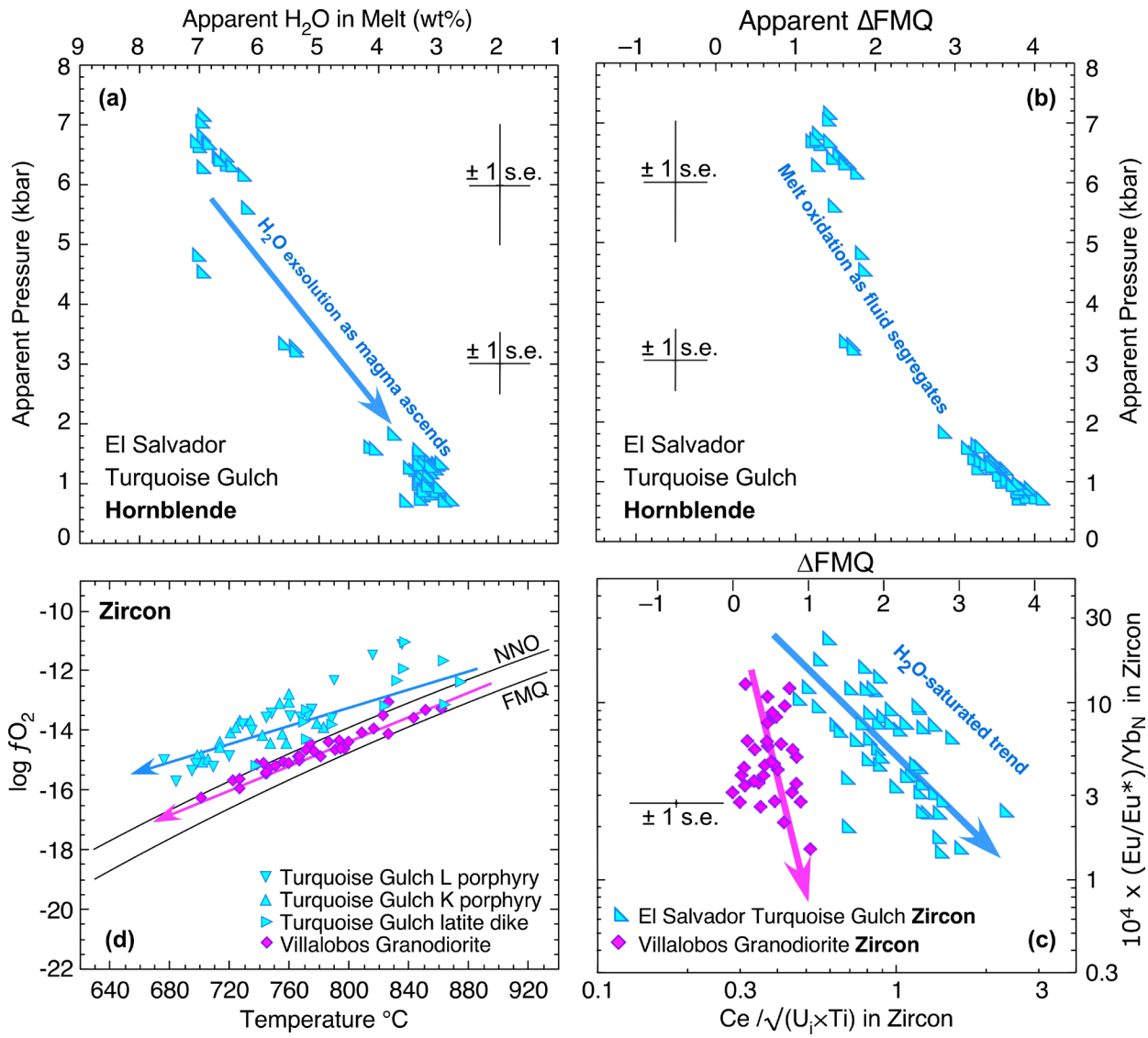

Fig. 3. Hornblende corroborates zircon oxybarometry and hygrometry trends; contrasting T–fO_2 trends of copper fertile and infertile arc magmas. (a) Al-in-hornblende barometry (calibration by Mutch et al., 2016; standard errors ±16%) and hornblende-based melt hygrometry (calibrated by Ridolfi et al., 2010, with their standard error) represent hydrothermal fluid exsolution during magma decompression from ~7 to ~0.5 kbar. Hornblende analyses are by Lee (2008). (b) Fluid exsolution and segregation from decompressing magma caused oxidation of residual melt, represented by $\Delta FMQ \equiv \log fO_{2(sample)} - \log fO_{2(FMQ)}$; hornblende oxybarometer calibration by Ridolfi et al. (2010). (c) Zircon $(Eu_N/Eu^*)/Yb_N$, an indicator of melt hydration state, and zircon $Ce/\sqrt{(U_i \times Ti)}$, an indicator of melt oxidation state, show the same trends as hornblende indicators of melt hydration and oxidation states. Note matching ranges of ΔFMQ recorded by hornblende and zircon during magma decompression. El Salvador zircon analyses are from Lee et al. (2017). Cores and rims of zircons in a late Neogene granodioritic intrusion in the Villalobos igneous complex were analyzed in this study. The standard error of ΔFMQ is ±0.6 log unit, as reported by Loucks et al. (2020). (d) Zircon oxybarometry and Ti-in-zircon thermometry by methods of Loucks et al. (2020) illustrate typical contrast in T–fO_2 arrays of PCD-related intrusions, as represented by the Turquoise Gulch porphyry copper deposit, and nonore-forming calc-alkalic arc suites as represented by Pliocene granodiorite in the Villalobos complex, central Chile. Trends of T–fO_2 evolution (arrows diverging from parental arc-basaltic magmas of similar initial oxidation state) are sensitive to relative hydration states of the zircon-saturated melts (Loucks et al., 2018). Notes: Shown for reference are oxygen fugacity buffers NNO (nickel metal + nickel oxide) and FMQ (fayalite + magnetite + quartz). The plotted hornblende and zircon analyses and derived parameters are listed in Appendix Table A3. Abbreviations: PCD = porphyry copper deposit, s.e. = standard error, T = temperature.

and chlorine concentrations, and greater metallogenic fertility. As described below, the effect of fluid/melt partitioning of sulfur is expected to be weaker than the effect of chlorine on the rate of Fe^{3+}/Fe^{2+} increase in residual melt and $Ce/\sqrt{(U \times Ti)}$ increase in zircon as fluid segregates.

Figure 3d shows the typical contrast in oxidation state of PCD-forming and barren calc-alkalic arc magmas as represented by comparison of El Salvador zircons analyzed by Lee et al. (2017) with our analyses of zircons in a nonore-forming late Neogene granodiorite intrusion in the Villalobos igne-

ous complex 1,100 km south of El Salvador. Our zircon oxybarometry herein (Figs. 3d, 4; App. Table A2) indicates that most PCD-forming granitoid melts have oxidation states near the sulfide/sulfate redox transition. Like magmas parental to many major PCDs worldwide, the El Salvador Turquoise Gulch K porphyry and latite dike (Fig. 3) contain magmatic anhydrite, indicating high SO_3 content of the ore-forming melts (Hutchinson and Dilles, 2019). The S^{6+} dissolution capacity of anhydrite-saturated hydrous granitoid melts is about an order of magnitude higher than their mss-saturated S^{2-} dissolution capacity (Luhr, 1990; Jugo, 2009). Experiments by Scaillet et al. (1998) on dacitic melt at 2.24 kbar and 780°C demonstrate that SO_2 is much more volatile than SO_3. Accordingly, S^{6+} in the silicate melt partitions into exsolving hydrothermal fluid mainly as S^{4+}, with concomitant oxidation of Fe (and Ce, V, and other redox couples) in residual melt: $\frac{1}{2}\ SO_{3(melt)} + Fe^{2+}O_{(melt)} \rightarrow Fe^{3+}O_{1.5(melt)} + \frac{1}{2}\ SO_{2(aqueous)}$. At subsolidus temperatures, aqueous SO_2 reacts with H_2O to make H_2S for precipitation of ore metals: $4\ SO_{2(aq)} + 4\ H_2O \rightarrow 3\ H_2SO_{4(aq)} + H_2S_{(aq)}$. Therefore, a shallower slope of zircon arrays in plots of $(Eu_N/Eu^*)/Yb_N$ vs. $Ce/\sqrt{(U_i \times Ti)}$ implies a higher rate of oxidation of residual melt per increment of fluid loss, which, in turn, implies greater sulfur availability in the granitoid melt and in exsolving magmatic-hydrothermal fluid, higher fluid/melt partition coefficients of $FeCl_2$ and CuCl complexes (Tattitch and Blundy, 2017), and the likelihood of more efficient copper precipitation in and near the fluid source. The relations described in this and the preceding paragraph indicate that the Fe^{3+}/Fe^{2+} ratio in residual melt varies with the square root of SO_2 concentration in exsolving fluid but varies with the square of Cl concentration in the fluid. The fluid's Cl concentration typically is greater than its S concentration and has a greater effect on the slope of a zircon array on plots like those in Figures 3c and 4, making variations of slope useful as indicators of the exsolving fluid's efficiency in scavenging CuCl from the silicate melt.

Two-Stage Evolution to High Oxidation State in Adakitic Arc Magmas

During precipitation of olivine and pyroxenes from mafic melts and precipitation of hornblende from andesitic and dacitic melts, Fe^{2+} is sequestered in cumulates relative to Fe^{3+}, promoting a tandem rise in the residual melt's ΔFMQ and wt % H_2O (Ulmer et al., 2018; Goltz et al., 2022; Rudra and Hirschmann, 2022). Accumulation of dissolved H_2O during magmatic differentiation also may raise the residual melt's Fe^{3+}/Fe^{2+} ratio and ΔFMQ by homogeneous equilibria of the type $\frac{1}{2}\ H_2O_m + Fe^{2+} + \frac{1}{4}\ O_2 = OH^- + Fe^{3+}$ wherein H_2O_m represents molecular water dissolved in the melt, and OH^- replaces a bridging oxygen linking Al and Si in the melt's tetrahedral framework (Loucks and Fiorentini, 2023b, and references therein). The melt's ratio H_2O_m/OH rises steeply with increasing total dissolved H_2O (Dixon et al., 1995), which promotes rising Fe^{3+}/Fe^{2+} in residual melt during fluid-undersaturated fractional crystallization of hydrous magmas. The positive correlation of a melt's oxidation state and hydration state during fluid-undersaturated fractional crystallization is inherited by zircon as a positive correlation of $Ce/\sqrt{(U_i \times Ti)}$ with $(Eu_N/Eu^*)/Yb_N$ in Figure 4.

Owing to positive dependence of H_2O solubility on load pressure in granitoid melts (Holtz et al., 1995), decompression during ascent typically is accompanied by onset of hydrothermal fluid exsolution at a depth that depends on the dissolved volatile contents of the melt. Melts having low contents of dissolved C-O-H-S volatiles begin to exsolve immiscible fluid at shallow depths, whereas the opposite is true of volatile-rich melts departing from high-pressure storage chambers where volatile components may have accumulated to high values during multiple cycles of chamber replenishment and fractional crystallization.

Exsolution of hydrothermal fluid from decompressing granitoid melts tends to be accompanied by channelized streaming of buoyant fluid and accumulation at the top of the ascending magma column where it is out of effective diffusive communication with its parent melt. The residual melt becomes more oxidized owing to the fluid's selective removal of reduced members of the principal redox couples in the melt: H_2–H_2O, S^{4+}–S^{6+}, and Fe^{2+}–Fe^{3+}. Experiments by Humphreys et al. (2015) demonstrate that the melt's selective loss of H_2 relative to H_2O as buoyant bubbles segregate from the melt oxidizes Fe in the residual melt: the reaction $2\ FeO_{(m)} + H_2O_{(m)} \rightarrow Fe_2O_{3(m)} + H_{2(aq)}$ is pulled to the right by selective extraction of H_2. Experiments by Scaillet et al. (1998) on dacitic melt at 2.24 kbar and 780°C show that S^{6+} in the silicate melt partitions into exsolving hydrothermal fluid mainly as S^{4+}, with concomitant oxidation of Fe in residual melt: $\frac{1}{2}\ S^{6+}_{(m)} + Fe^{2+}_{(m)} \rightarrow \frac{1}{2}\ S^{4+}_{(aq)} + Fe^{3+}_{(m)}$, which is pulled to the right as SO_2-bearing fluid segregates. Experiments by Bell and Simon (2011) show that Fe^{2+} partitions into chloride-bearing magmatic hydrothermal fluid much more strongly than Fe^{3+}, with the result that fractional segregation of buoyant brine raises the Fe^{3+}/Fe^{2+} (i.e., ΔFMQ) of residual melt.

Ascent of volatile-rich magma from a Moho-vicinity gestation chamber tends to be accompanied by the onset of fluid exsolution and plagioclase precipitation in response to decompression (Loucks 2021; Loucks and Fiorentini, 2023b), which in turn drives coprecipitation of hornblende, apatite, and zircon as the melt becomes residually enriched in components of those minerals. As zircon and plagioclase coprecipitate while hydrothermal fluid is exsolving and segregating from decompressing melt, these processes produce a negative correlation of the zircon $(Eu_N/Eu^*)/Yb_N$ indicator of melt hydration state and the zircon $Ce/\sqrt{(U_i \times Ti)}$ indicator of melt oxidation state, represented by down-to-the-right arrows in Figure 4 and negatively sloping arrays in Figures 3c and 5a.

Zircon Discriminants of Copper Ore-Forming and Barren Arc Igneous Suites

Figure 4 is a plot of 5,777 zircon compositions compiled from our own and other publications. Appendix 1 describes selection criteria. The analyses and their literature sources and derived composition parameters are listed in Appendix Table A2 for readers wanting to examine individual suites in isolation. The data set includes 2,220 zircons from intrusions inferred by the respective authors to have exsolved ore-forming magmatic-hydrothermal fluids in 37 major magmatic-hydrothermal Cu-rich ore deposits of Phanerozoic age worldwide. Those are compared to 3,557 zircons from non-ore-forming magmas at Phanerozoic convergent plate margins. It is evi-

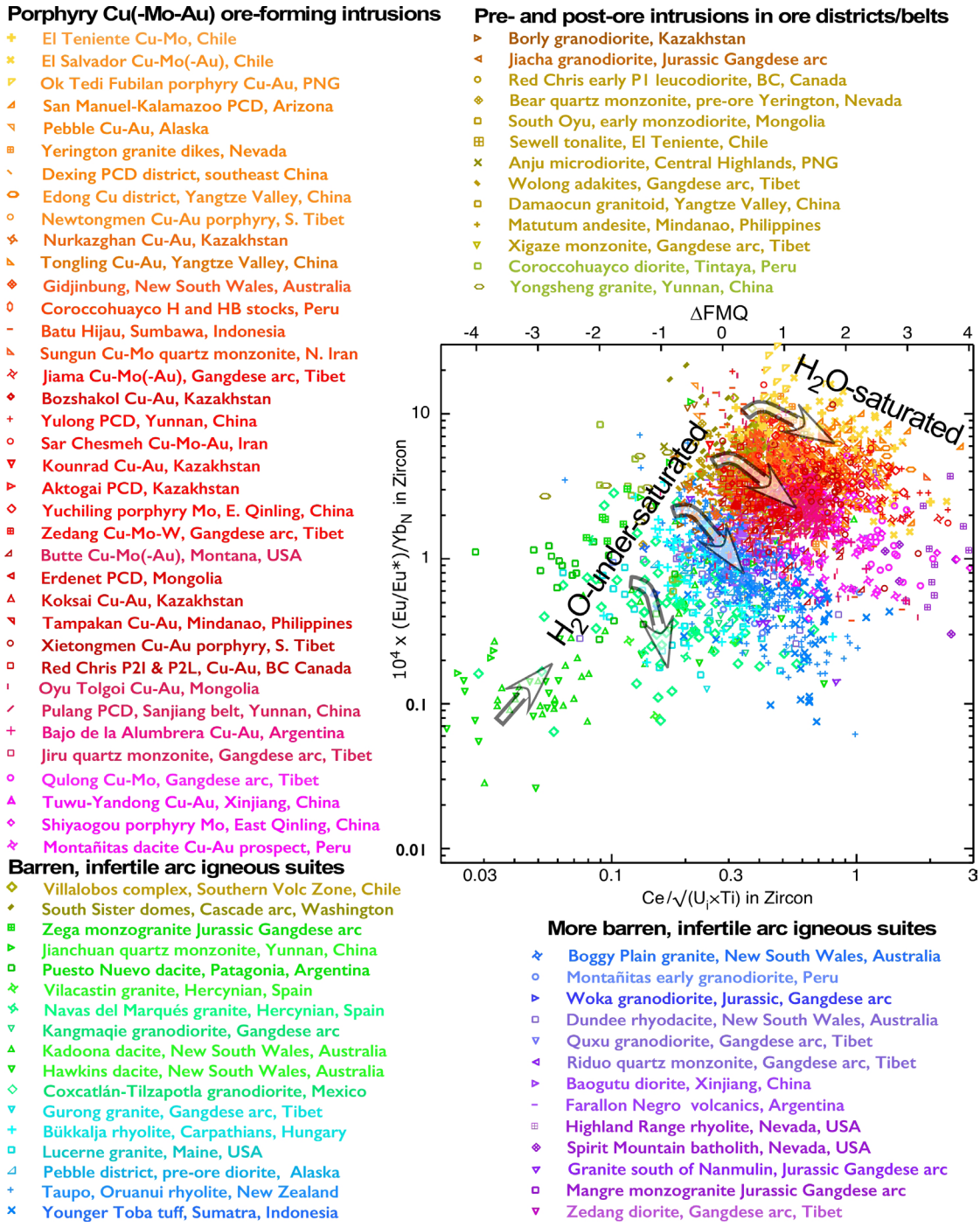

Fig. 4. Zircon discriminants of magmatic copper fertility for 5,777 zircon analyses from 80 ore-bearing and unmineralized subduction-related igneous suites. Zircon Ce/(U_i × Ti) increases as the parent melt's relative oxidation state (ΔFMQ) increases. Zircon $(Eu_N/Eu^*)/Yb_N$ increases with lithostatic pressure and dissolved wt % H_2O in the melt. Zircons from PCD-forming intrusions are orange and red symbols. Tan symbols are zircons in pre- and post-ore intrusions in ore-hosting igneous complexes. Green, turquoise, blue, and purple symbols are barren arc igneous suites. Arrows schematically represent the turn in trajectory in melt and zircon composition at the transition from fluid-undersaturated magmatic differentiation (positive slope) to fluid-saturated evolution (negative slope) in granitoid melts of varied volatile content at onset of fluid saturation. In low-H_2O melts infertile for Cu metallogeny, the rising zircon trend rolls over at lower $(Eu_N/Eu^*)/Yb_N$ and lower ΔFMQ than in H_2O-rich, metallogenically fertile melts in which the zircon trend rolls over at high $(Eu_N/Eu^*)/Yb_N$ and high ΔFMQ. Zircon growth while hydrothermal fluid exsolves from decompressing, dehydrating melt produces the trends having negative slopes (as in Figs. 3c and 5a) that vary with Cl and S concentrations in the exsolving hydrothermal fluid. Zircon analyses and literature sources are listed in Appendix Table A2, which provides a template for calculation of Ce/(U_i × Ti), ΔFMQ, log $f_{O_{2(sample)}}$, $(Eu_N/Eu^*)/Yb_N$, Ti-in-zircon temperature, and other parameters. Abbreviations: FMQ = fayalite + magnetite + quartz, PCD = porphyry copper deposit.

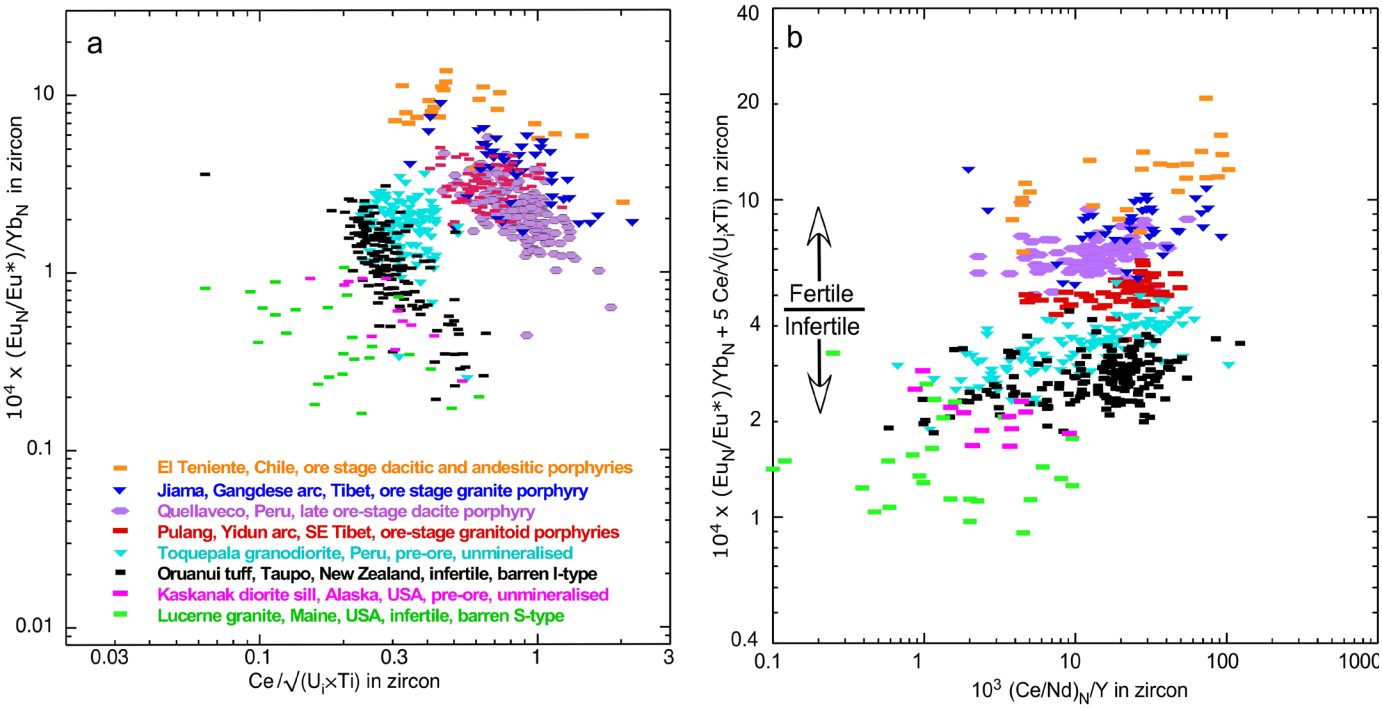

Fig. 5. (a) Compositional heterogeneity within and among cognate, zoned zircons imparts dispersion to zircon arrays, so microbeam analyses of zircons in a single intrusion or hand specimen commonly span a 10-fold range in $(Eu_N/Eu^*)/Yb_N$, with substantial overlap in the $(Eu_N/Eu^*)/Yb_N$ ranges of fertile and infertile intrusions, as well as a substantial range in $Ce/\sqrt{(U_i \times Ti)}$. (b) Zircons from ore-stage intrusions in four porphyry copper deposits (El Teniente, Jiama, Quellaveco, and Pulang) are compared with zircons in pre-ore intrusions (Toquepala Granodiorite in Peru and Kaskanak diorite in the Pebble district, Alaska), and in infertile igneous units in unmineralized regions (Oruanui rhyolite tuff, Lucerne granite). The compound fertility index (ordinate axis) in (b) compresses the range of each zircon population to ~two-fold variation as compared to ~10-fold range in $(Eu_N/Eu^*)/Yb_N$ arrays of individual igneous units in panel (a), and the compound zircon copper fertility index (ZCFI), in (b) eliminates nearly all overlap in the ordinate-axis ranges of fertile and infertile zircon suites. A ZCFI cutoff value near 4.5 distinguishes most zircons in ore-forming intrusions from most zircons in nonmineralizing igneous units. All plotted data and literature sources are listed in Appendix Table A2. The ratio $(Ce/Nd)_N/Y$ tends to increase with increasing hydration state and decreasing temperature of the magmatic differentiation series.

dent that these composition parameters in zircon effectively discriminate metallogenically fertile magmas from infertile ones. Zircons that plot in the upper-right sector of Figure 4 (orange and red field) are empirically diagnostic of magmatic copper metallogenic fertility. Fanning slopes of down-to-the-right arrows (fluid-saturated trends) further discriminate ore-productive from less fertile intrusions by indicating variation among intrusions in the rate of residual melt oxidation as hydrothermal fluid exsolved and escaped, which, in turn, indicate variation among intrusions in the chlorine (and sulfur) content of exsolving fluid. So, both position and slope of a magma's zircon array on this type of plot are indicators of Cu(-Au-Mo) ore-forming fertility.

In the literature on zircon trace element composition, there has been widespread misinterpretation of the links between zircon composition and silicate melt composition. In zircon, Ce^{4+}/Ce^{3+}, Ce/Ce^*, Ce/Nd, and Eu/Eu^* have weak significance as magmatic redox indicators because of extreme sensitivity to and domination by temperature-dependent lattice strain, which is increasingly selective for the smaller (higher valence) ions in Zr^{4+} lattice sites at lower temperatures. Data from experiments and natural assemblages indicate that cooling from 1,300° to 700°C causes the ratios of zircon/melt partition coefficients $D_{Eu^{3+}}^{zirc/melt}/D_{Eu^{2+}}^{zirc/melt}$ and $D_{Ce^{4+}}^{zirc/melt}/D_{Ce^{3+}}^{zirc/melt}$ to increase by ~4 orders of magnitude in a narrow range of ΔFMQ (Loucks et al., 2018; Loucks and Fiorentini, 2023b, and references therein). The temperature at which a crystallizing silicate melt accumulates enough residual Zr to attain zircon saturation is strongly dependent on the hydration state of the melt, so those Ce and Eu redox ratios in zircon are overwhelmingly dominated by coupled T-P_{H_2O} effects not melt redox.

The plotting coordinates in Figures 3c and 4 sort the effects of melt oxidation state and hydration state and clarify their roles. A valid indicator of the oxidation state of a silicate melt (and exsolving fluid) provides a valid indicator of its sulfur-carrying capacity, which is a metallogenic fertility indicator. Zircon analyses that plot in the upper-right quadrant of Figure 4 crystallized from exceptionally H_2O-rich silicate melts, which had enough H_2O (and accompanying volatiles) to begin exsolving hydrothermal fluid at lower- to mid-crustal pressures (Fig. 3a, b) at which exsolving fluid has high $D_{Cl}^{fluid/melt}$ and thus high efficacy in scavenging Cu and other chloride-complexed metals from the silicate melt. This clarification of roles of trace element ratios in zircon permits recognition that variation among slopes of zircon arrays is an indicator of chlorine concentration in segregating hydrothermal fluid, and hence, of the fluid's Cu-scavenging efficacy and metallogenic fertility. H_2O and Cl con-

tents of melts and exsolving fluids are not rigidly coupled, so having two quasi-independent indicators (position and slope of zircon arrays on plots like Figs. 3c and 4) is useful.

Readers who would like to compare slopes and positions of their zircon arrays with those from intrusions that produced giant PCDs can plot theirs in comparison with reference suites for El Teniente, Ok Tedi, El Salvador, Pebble, or others, in Appendix Table A2.

Cu Fertile/Infertile Cut Off for a Compound Fertility Indicator Useful for Detrital Zircons

Figures 3c and 5a show that zircon grain populations from individual igneous units or single hand specimens commonly have $(Eu_N/Eu^*)/Yb_N$ values that span an order of magnitude caused by zircon growth over a 10- to 30-km depth interval during magma decompression and fluid exsolution (Fig. 3a-c). Values for $Ce/\sqrt{(U_i \times Ti)}$ also span a substantial range owing to compositional zoning within crystals and because not all cognate crystals within a sample nucleated simultaneously from compositionally evolving melt during magma storage and ascent. The large range of values of $(Eu_N/Eu^*)/Yb_N$ and $Ce/\sqrt{(U_i \times Ti)}$ in and among zoned zircons within single intrusions impedes confident fertility assessment. Improving the statistical confidence level of fertility assessments by analyzing large numbers of zircon grains in sediment samples raises the cost of applying this exploration method. Therefore, we introduce a composite index that compresses the range of variation within a cogenetic grain population and decreases the number of zircon analyses needed for prospectivity assessment.

Zircon grain populations from individual igneous units in Figures 3c, 4, and 5a have slopes wherein $(Eu_N/Eu^*)/Yb_N$ decreases at two to 10 times the rate at which $Ce/\sqrt{(U_i \times Ti)}$ increases—about five times on average. A generally applicable zircon copper fertility index (ZCFI) that can be applied to each microbeam spot analysis is:

$$ZCFI = 10^4 (Eu_N/Eu_N^*)/Yb_N + 5\ Ce/\sqrt{(U_i \times Ti)} \quad (1)$$

For comparison with the ~8- to 10-fold ranges of $(Eu_N/Eu^*)/Yb_N$ within individual grain populations in Figure 5a, Figure 5b shows that this compound parameter flattens the ordinate-axis range of each zircon population to about a factor of two and eliminates nearly all overlap in the ranges of individual populations of Cu-fertile and Cu-infertile zircons. This compression permits fewer analyses to capture the fertile/infertile characteristics of the parental magma, thereby reducing the cost of applying the method to detrital zircons in sediment samples. In the abscissa variable, $(Ce/Nd)_N/Y$, the ratio Ce/Nd represents the amplitude of the Ce spike, which tends to rise with increasing hydration state and decreasing temperature of the magmatic differentiation series; the denominator, parts per million Y, tends to decrease with increasing cumulative proportion of hornblende in the differentiation series of more hydrous melts.

Example of Application of Detrital Zircons to Identification of Copper Exploration Targets

Lee et al. (2021) report compositions of zircons recovered from glacial till samples downstream from the Guichon Creek composite batholith (British Columbia), which contains the Highland Valley porphyry copper district comprising several economically important deposits (Fig. 6a). See the report by Lee et al. (2021) for a description of district geology and sample collection and analytical procedures by laser ablation-inductively coupled plasma-mass spectrometry (LA-ICP-MS). Figure 6, parts b and c, illustrate application of our zircon composition parameters to recognition of stream drainages containing Cu-mineralized and unmineralized regions of the batholith. Successively younger intrusions emplaced inward from the unmineralized border zone grade toward increasing Cu fertility. Ice streams that passed over PCDs in the core of the batholith sampled unmineralized intervals upstream and downstream from the deposits, so each such till sample contains zircons spanning a range of ZCFI. Samples downstream from the unmineralized border zone contain no conspicuously Cu-prospective zircons. Till samples downstream from the interior unmineralized zone span a range overlapping prospective values of ZCFI. Till samples downstream from ore-forming intrusions in the batholith core contain a large proportion of highly Cu-prospective ZCFI values. Appendix Table A4 lists the compositions of all analyzed zircons in all till samples, including fertility indicators and $\log f_{O_2}$ and ΔFMQ and $Ce/\sqrt{(U_i \times Ti)}$ values corrected for an error by Lee et al. (2021) in calculating decay-corrected initial parts per million U, which caused significant underestimates of ΔFMQ, rendering it seemingly uninformative as a fertility indicator.

Figure 3c and Appendix Table A3 show that zircons in intrusions that generated the giant Turquoise Gulch deposit and zircons in the insignificantly mineralized Villalobos intrusion have similar ranges of Eu/Eu*, so the Eu anomaly alone (used by Lee et al., 2021, as a default metallogenic fertility indicator in their Guichon batholith study) is not a sufficiently sensitive or reliable indicator of magmatic metallogenic fertility. The parameter $(Ce/Nd)_N/Y$ in zircon (Fig. 5c) was introduced by Lu et al.(2016) as a qualitative indicator of silicate melt hydration state, but zircon Ce/Nd is actually a lattice-strain-based qualitative thermometer (like Ce^{4+}/Ce^{3+} and Ce/Ce*) that reflects the effect of dissolved H_2O in lowering the temperature at which the melt accumulates enough Zr to attain zircon saturation. As a melt hygrometer, $(Ce/Nd)_N/Y$ is not as sensitive as $(Eu_N/Eu^*)/Yb_N$. Use of the composite ZCFI indicator of magmatic Cu metallogenic fertility (Fig. 5b and 6c) enhances resolution of ore-forming fertility for petrologically well understood reasons.

Owing to the mechanical and chemical robustness of zircon, the watershed-scale footprint of this diagnostic tool is much larger than the detection range of conventional geochemical sampling techniques and is applicable to paleo-watersheds. In application to paleo-drainages, it may identify areas containing fertile igneous complexes that formerly were exposed to erosion but are now buried under younger volcanic or sedimentary cover. It is feasible to do about 500 spot analyses per day by LA-ICP-MS on grain mounts of detrital zircons, making it cost-competitive with other geochemical exploration strategies.

Conclusions

Trace element features of zircons and whole-rock samples that are diagnostic of unusually high hydration and oxidation states of their parent silicate melt effectively discriminate Cu-ore-forming igneous complexes from ordinary, unmineralized arc igneous suites. In zircon, Eu/Eu*, Ce/Ce*, and Ce^{4+}/Ce^{3+}

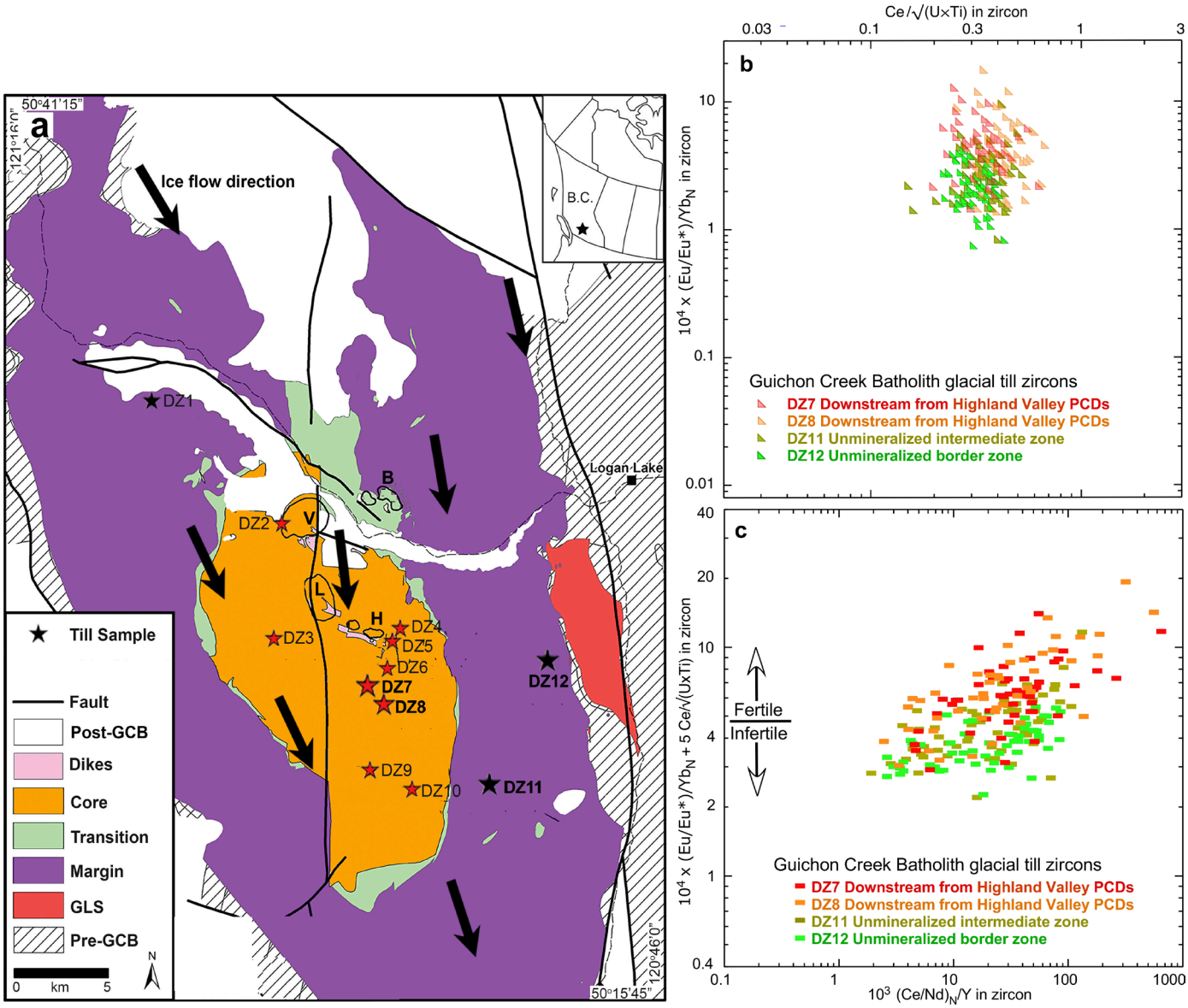

Fig. 6. (a) Simplified bedrock map of the Guichon Creek Batholith (GCB; modified after Lee et al., 2021) showing ice flow directions (black arrows) and locations of their glacial till samples with respect to major PCDs) of the Highland Valley district in the core zone of the batholith. The inset shows the location of the project area in southcentral British Columbia (B.C.). (b) Zircon trace element indicators of magmatic oxidation state and hydration state in GCB-derived Triassic zircons analyzed by Lee et al. (2021) in selected till samples downstream from unmineralized and mineralized zones of the batholith. See Appendix Table A3 for all zircon compositions and fertility indicators of all till samples. (c) Zircon copper fertility index plotted against an alternative zircon indicator of magmatic hydration state, (Ce/Nd)/Y, for the same till samples as in panel (b). B = Bethlehem deposit, GLS = Gump Lake stock, H = Highmont deposit, L = Lornex deposit, PCD = porphyry copper deposit, V = Valley deposit.

have been widely misconstrued as magmatic redox indicators (e.g., Ballard et al., 2002), but they are actually lattice-strain-based qualitative hygrometer-thermometers that tend to increase with decreasing temperature, because increasing dissolved H_2O depresses the temperatures at which residual melts accumulate enough Zr to attain zircon saturation, and thermal contraction of the zircon lattice causes zircon crystallizing at lower temperatures to be increasingly selective for the higher-valence, smaller ion in a redox pair. The ratio $Ce/\sqrt{(U_i \times Ti)}$ in zircon is a well-calibrated, precise measure of relative oxidation state (ΔFMQ) of the zircon's parent melt, which can be used with Ti-in-zircon thermometry (revised by Loucks et al., 2020) in application to rock-hosted zircons or a tightly age-clustered subpopulation of detrital zircons to retrieve T vs. f_{O_2} trends of melt evolution during magmatic differentiation (Figure 3d).

On a plot of zircon $(Eu_N/Eu^*)/Yb_N$ vs. $Ce/\sqrt{(U_i \times Ti)}$, zircons precipitating from fluid-undersaturated, plagioclase-saturated melt plot as a downward-directed, subvertical array (fig. 6 of Loucks and Fiorentini, 2023b); zircons precipitating

from fluid-undersaturated, plagioclase-undersaturated melt evolve along a rising trend of positive slope (Fig. 4), whereas zircons precipitating from fluid-saturated, plagioclase-saturated melt evolve along trends of negative slope that varies mainly with chlorinity of the segregating hydrothermal fluid (and, with less sensitivity, varies with SO_2 content of segregating fluid). Shallower slopes represent higher chlorinity and indirectly imply a higher fluid/melt partition coefficient of Cu and greater Cu-scavenging efficiency by segregating hydrothermal fluid. Figure 4 shows that zircons from most PCD-forming intrusions record melt redox states near the sulfide/sulfate redox transition at $\Delta FMQ \approx 1.5 \pm 0.5$, which maximizes the S content of exsolving hydrothermal fluid. These quantitative indicators of magmatic temperature and oxidation state, and qualitative indicators of melt hydration state and of chloride and sulfur contents of exsolving hydrothermal fluid are applicable to detrital zircons, which may provide cost-effective identification of (paleo)watersheds containing exposed or formerly exposed, now covered Cu-rich magmatic-hydrothermal ore deposits upstream from the sediment sampling site.

Acknowledgments

We thank Charlotte Allen for assistance analyzing Villalobos zircons. We thank Paul Agnew of Rio Tinto Exploration and Cam McCuaig and Natalie Caciagli of BHP Exploration for encouragement and helpful discussions. G.J.H. thanks BHP for support during his Ph.D. program, of which this work is a part. We thank Peter Hollings and David Cooke for thoughtful, detailed reviews that led to substantial improvements of the manuscript, including a recommendation to incorporate the Highland Valley detrital zircon case study.

REFERENCES

Arató, R., and Audétat, A., 2017, Experimental calibration of a new oxybarometer for silicic magmas based on vanadium partitioning between magnetite and silicate melt: Geochimica et Cosmochimica Acta, v. 209, p. 284–295,doi: 10.1016/j.gca.2017.04.020.

Arndt, N.T., Fontboté, L., Hedenquist, J.W., Kesler, S.E., Thompson, J.F.H., and Wood, C.G., 2017, Future global mineral resources: Geochemical Perspectives, v. 6, p. 1–171, doi: 10.7185/geochempersp.6.1.

Audétat, A., and Pettke, T., 2006, Evolution of a porphyry-Cu mineralized magma system at Santa Rita, New Mexico (USA): Journal of Petrology, v. 47, p. 2021–2046, doi: 10.1093/petrology/egl035.

Ballard, J.R., Palin, M.J., and Campbell, I.H., 2002. Relative oxidation states of magmas_inferred from Ce (IV)/Ce (III) in zircon: Application to porphyry copper deposits of northern Chile: Contributions to Mineralogy and Petrology, v. 144, p. 347–364, doi: 10.1007/s00410-002-0402-5.

Bell, A.S., and Simon, A., 2011, Experimental evidence for the alteration of the $Fe^{3+}/\Sigma Fe$ of silicate melt caused by the degassing of chlorine-bearing aqueous volatiles: Geology, v. 39, p. 499–502, doi: 10.1130/G31828.1.

Blundy, J., Cashman, K.V., Rust, A., and Witham, F., 2010, A case for CO_2-rich arc magmas: Earth and Planetary Science Letters, v. 290, p. 289–301, doi: 10.1016/j.epsl.2009.12.013.

Botcharnikov, R.E., Holtz, F., and Behrens, H., 2015, Solubility and fluid-melt partitioning of H_2O and Cl in andesitic magmas as a function of pressure between 50 and 500 MPa: Chemical Geology, v. 418, p. 117–131, doi: 10.1016/j.chemgeo.2015.07.019.

Dixon, J.E., Stolper, E.M., and Holloway, J.R., 1995, An experimental study of water and carbon dioxide solubilities in mid-ocean ridge basaltic liquids. Part I. Calibration and solubility models: Journal of Petrology, v. 36, p. 1607–1631, doi: 10.1093/oxfordjournals.petrology.a037268.

Du, J., and Audétat, A., 2020, Early sulfide saturation is not detrimental to porphyry Cu-Au formation: Geology, v. 48, p. 519–524, doi: 10.1130/G47169.1.

Fiorentini, M.L., and Garwin, S.L., 2010, Evidence of a mantle contribution in the genesis of magmatic rocks from the Neogene Batu Hijau district in the Sunda arc, southwestern Sumbawa, Indonesia: Contributions to Mineralogy and Petrology, v. 159, p. 819–837, doi: 10.1007/s00410-009-0457-7.

Fortin, M.-A., Riddle, J., Desjardins-Langlais, Y., and Baker, D.R., 2015, The effect of water on the sulfur concentration at sulfide saturation (SCSS) in natural melts: Geochimica et Cosmochimica Acta, v. 160, p. 100–116, doi: 10.1016/j.gca.2015.03.022.

Goltz, A.E., Krawczynski, M.J., McCanta, M.C., and Dyar, M.D., 2022, Experimental calibration of an Fe^{3+}/Fe^{2+}-in-amphibole oxybarometer and its application to shallow magmatic processes at Shiveluch volcano, Kamchatka: American Mineralogist, v. 107, p. 2084–2100, doi: 10.2138/am-2022-8031.

Grondahl, C., and Zajacz, Z., 2022, Sulfur and chlorine budgets control the ore fertility of arc magmas: Nature Communications, v. 13, article 4218, doi: 10.1038/s41467-022-31894-0.

Holtz, F., Behrens, H., Dingwell, D.B., and Johannes, W., 1995, H_2O solubility in haplogranitic melts: Compositional, pressure, and temperature dependence: American Mineralogist, v. 80, p. 94–108, doi: 10.2138/am-1995-1-210.

Hsu, Y.-J., Zajacz, Z., Ulmer, P., and Heinrich, C.A., 2019, Chlorine partitioning between granitic melt and H_2O-CO_2-NaCl fluids in the Earth's upper crust and implications for magmatic-hydrothermal ore genesis: Geochimica et Cosmochimica Acta, v. 261, p. 171–190, doi: 10.1016/j.gca.2019.07.005.

Humphreys, M.C.S., Brooker, R.A., Fraser, D.G., Burgisser, A., Mangan, M.T., and McCammon, C., 2015, Coupled interactions between volatile activity and Fe oxidation state during arc crustal processes: Journal of Petrology, v. 56, p. 795–814, doi: 10.1093/petrology/egv017.

Hutchinson, M.C., and Dilles, J.H., 2019, Evidence for magmatic anhydrite in porphyry copper intrusions: Economic Geology, v. 114, p. 143–152, doi: 10.5382/econgeo.2019.4624

International Energy Agency, 2021, The role of critical minerals in clean energy transitions: World Energy Outlook Special Report, https://www.iea.org/reports/the-role-of-critical-minerals-in-clean-energy-transitions.

Jugo P.J., 2009, Sulfur content at sulfide saturation in oxidized magmas: Geology, v. 37, p. 415–418, doi: 10.1130/G25527A.1.

King, P.L., Hervig, R.L., Holloway, J.R., Delaney, J.S., and Dyar, M.D., 2000, Partitioning of Fe^{3+}/Fe_{total} between amphibole and basanitic melt as a function of oxygen fugacity: Earth and Planetary Science Letters, v. 178, p. 97–112, doi: 10.1016/S0012-821X(00)00071-6.

Lee, R.G., 2008, Genesis of the El Salvador porphyry copper deposit, Chile and distribution of epithermal alteration at Lassen Peak, California: Ph.D. thesis, Corvallis, Oregon, Oregon State University, 344 p.

Lee, R.G., Dilles, J.H., Tosdal, R.M., Wooden, J.L., and Mazab, F.K., 2017, Magmatic evolution of granodiorite intrusions at the El Salvador porphyry copper deposit, Chile, based on trace element composition and U/Pb age of zircons: Economic Geology, v. 112, p. 245–273, doi: 10.2113/econgeo.112.2.245.

Lee, R.G., Plouffe, A., Ferbey, T., Hart, C.J.R., Hollings, P., and Gleeson, S.A., 2021, Recognizing porphyry copper potential from till zircon composition: A case study from the Highland Valley porphyry district, south-central British Columbia: Economic Geology, v. 116, p.1035–1045, doi: 10.5382/econgeo.4808.

Loucks, R.R., 2014, Distinctive composition of copper-ore-forming arc magmas: Australian Journal of Earth Sciences, v. 61, p. 5–16, doi: 10.1080/08120099.2013.865676.

——2021, Deep entrapment of buoyant magmas by orogenic tectonic stress: Its role in producing continental crust, adakites, and porphyry copper deposits: Earth Science Reviews, v. 220, article 103744, doi: 10.1016/j.earscirev.2021.103744.

Loucks, R.R. and Fiorentini, M.L., 2023a, Early zircon saturation in adakitic magmatic differentiation series and low Zr content of porphyry copper magmas: Mineralium Deposita, v. 58, p. 1381–1393, doi: 10.1007/s00126-023-01208-5.

——2023b, Oxidation of magmas during gain and loss of H_2O recorded by trace elements in zircon: Earth and Planetary Science Letters, v. 622, article 118377, doi: 10.1016/j.epsl.2023.118377.

Loucks, R.R., Fiorentini, M.L., and Rohrlach, B.D., 2018, Divergent T–fO_2 paths during crystallisation of H_2O-rich and H_2O-poor magmas as recorded by Ce and U in zircon, with implications for TitaniQ and TitaniZ geothermometry: Contributions to Mineralogy and Petrology, v. 173, article 104, doi: 10.1007/s00410-018-1529-3.

Loucks, R.R., Fiorentini, M.L., and Henriquez, G.J., 2020, New magmatic oxybarometer using trace elements in zircon: Journal of Petrology, v. 61, article egaa034, doi: 10.1093/petrology/egaa034.

Lu, Y.-J., Loucks, R.R., Fiorentini, M.L., McCuaig, T.C., Evans, N.J., Yang, Z.-M., Hou, Z.-Q., Kirkland, C.L., Parra-Avila, L.A., and Kobussen, A., 2016, Zircon compositions as a pathfinder for porphyry Cu ± Mo ± Au deposits: Society of Economic Geologists, Special Publication 19, p. 329–347, doi: 10.5382/SP.19.13.

Luhr, J.F., 1990, Experimental phase relations of water- and sulfur-saturated arc magmas and the 1982 eruptions of El Chichón volcano: Journal of Petrology, v. 31, p. 1071–1114, doi: 10.1093/petrology/31.5.1071.

Macpherson, C.G., Dreher, S.T., and Thirlwall, M.F., 2006, Adakites without slab melting: High pressure differentiation of island arc magma, Mindanao, the Philippines: Earth and Planetary Science Letters, v. 243, p. 581–593, doi: 10.1016/j.epsl.2005.12.034.

Martiny, B.M., Morán-Zenteno, D.J., Solari, L., López-Martínez, M., de Silva, S.L., Flores-Huerta, D., Zúñiga-Lagunes, L., and Luna-González, L., 2013, Caldera formation and progressive batholith construction: Geochronological, petrographic and stratigraphic constraints from the Coxcatlán-Tilzapotla area, Sierra Madre del Sur, Mexico: Revista Mexicana de Ciencias Geológicas, v. 30, p. 247–267.

Matjuschkin V., Blundy J.D., and Brooker, R.A., 2016, The effect of pressure on sulphur speciation in mid- to deep-crustal arc magmas and implications for the formation of porphyry copper deposits: Contributions to Mineralogy and Petrology, v. 171, article 66, doi: 10.1007/s00410-016-1274-4.

Moore, G., and Carmichael, I.S.E., 1998, The hydrous phase equilibria (to 3 kbar) of an andesite and basaltic andesite from western Mexico: Constraints on water content and conditions of phenocryst growth: Contributions to Mineralogy and Petrology, v. 130, p. 304–319, doi: 10.1007/s004100050367.

Mori, L., Morán-Zenteno, D.J., Martiny, B.M., González-Torres, E.A., Chapela-Lara, M., Díaz-Bravo, B., and Roberge, J., 2012, Thermomechanical maturation of the continental crust and its effects on the late Eocene-early Oligocene volcanic record of the Sierra Madre del Sur Province, southern Mexico: International Geology Review, v. 54, p. 1475–1496, doi: 10.1080/00206814.2011.644745.

Mutch, E.J.F., Blundy, J.D., Tattitch, B.C., Cooper, F.J., and Brooker, R.A., 2016, An experimental study of amphibole stability in low-pressure granitic magmas and a revised Al-in-hornblende geobarometer: Contributions to Mineralogy and Petrology, v. 171, article 85, doi: 10.1007/s00410-016-1298-9.

Nandedkar, R.H., Hürlimann, N., Ulmer, P., and Müntener, O., 2016, Amphibole-melt trace element partitioning of fractionating calc-alkaline magmas in the lower crust: An experimental study: Contributions to Mineralogy and Petrology, v. 171, article 71, doi: 10.1007/s00410-016-1278-0.

Naney, M.T., 1983, Phase equilibria of rock-forming ferromagnesian silicates in granitic systems: American Journal of Science, v. 283, p. 993–1033.

Nathwani, C.L., Simmons, A.T., Large, S.J.E., Wilkinson, J.J., Buret, Y., and Ihlenfeld, C., 2021, From long-lived batholith construction to giant porphyry copper deposit formation: Petrological and zircon chemical evolution of the Quellaveco district, southern Peru: Contributions to Mineralogy and Petrology, v. 176, article 12, doi: 10.1007/s00410-020-01766-1.

O'Hara, M.J., Mathews, R.E., 1981, Geochemical evolution in an advancing, periodically_replenished, periodically tapped, continuously fractionated magma chamber: Journal of the Geological Society (London) v. 138, p. 237–277, doi: 10.1144/gsjgs.138.3.0237.

Ridolfi, F., Renzulli, A., and Puerini, M., 2010, Stability and chemical equilibrium of amphibole in calc-alkaline magmas: An overview, new thermobarometric formulations and application to subduction-related volcanoes: Contributions to Mineralogy and Petrology, v. 160, p. 45–66, doi: 10.1007/s00410-009-0465-7.

Rohrlach, B.D., and Loucks, R.R., 2005, Multi-million-year ramp-up of volatiles in a lower-crustal magma reservoir trapped below the Tampakan copper-gold deposit by Mio-Pliocene crustal compression in the southern Philippines: *in* Porter, T.M., ed., Super porphyry copper and gold deposits—a global perspective, v.2; Adelaide, PCG Publishing, p. 369–407.

Rudra, A., and Hirschmann, M.M., 2022, Fe^{3+} partitioning between clinopyroxene and silicate melt at 1-2.5 GPa: Implications for Fe^{3+} content of MORB and OIB source mantle: Geochimica et Cosmochimica Acta, v. 328, p. 258–279, doi: 10.1016/j.gca.2022.04.023.

Scaillet, B., Clemente, B., Evans, B., and Pichavant, M., 1998, Redox control of sulfur degassing in silicic magmas: Journal of Geophysical Research, v. 103, p. 23,937–23,949, doi: 10.1029/98JB02301.

Sellés Mathieu, D.F., 2006, Stratigraphy, petrology, and geochemistry of Nevado de Longaví volcano, Chilean Andes (36.2°S): Ph.D. thesis, Geneva, Switzerland, Université de Genève, 103 p.

Shannon, R.D., 1976, Revised effective ionic radii and systematic studies of interatomic distances in halides and chalcogenides: Acta Crystallographica, v. A32, p. 751–767, doi: 10.1107/S0567739476001551.

Sillitoe, R.H., 2010, Porphyry copper systems: Economic Geology, v. 105, p. 3–41, doi: 10.2113/gsecongeo.105.1.3.

Stern, C.R., Skewes, A., and Arévalo, A., 2011, Magmatic evolution of the giant El Teniente Cu-Mo deposit, central Chile: Journal of Petrology, v. 52, p. 1591–1617, doi: 10.1093/petrology/egq029.

Tatnell, L., Anenburg, M., and Loucks, R., 2023, Porphyry copper deposit formation: Identifying garnet and amphibole fractionation with REE pattern curvature modeling: Geophysical Research Letters, v. 50, article e2023GL103525, doi: 10.1029/2023GL103525.

Tattitch, B.C., and Blundy, J.D., 2017, Cu-Mo partitioning between felsic melts and saline-aqueous fluids as a function of X_{NaCleq}, f_{O_2}, and f_{S_2}: American Mineralogist, v. 102, p. 1987–2006, doi: 10.2138/am-2017-5998.

Tattitch, B.C., Chelle-Michou, C., Blundy, J., and Loucks, R.R., 2021, Chemical feedbacks during magma degassing control chlorine partitioning and metal extraction in volcanic arcs: Nature Communications, v. 12, article 1774, doi: 10.1038/s41467-021-21887-w.

Ulmer, P., Kaegi, R., and Müntener, O., 2018, Experimentally derived intermediate to silica-rich arc magmas by fractional and equilibrium crystallization at 1.0 GPa: Evaluation of phase relationships, compositions, liquid lines of descent and oxygen fugacity: Journal of Petrology, v. 59, p. 11–58, doi: 10.1093/petrology/egy017.

Valencia, V.A., Ruiz, J., Barra, F., Geherls, G., Ducea, M., Titley, S.R., and Ochoa-Landin, L., 2005, U-Pb zircon and Re-Os molybenite geochronology from La Caridad porphyry copper deposit: Insights for the duration of magmatism and mineralization in the Nacozari district, Sonora, Mexico: Mineralium Deposita, v. 40, p. 175–191, doi: 10.1007/s00126-005-0480-1.

Wallace, P.J., Plan, T., Bodnar, R.J., Gaetani, G.A., Shea, T., 2021, Olivine-hosted melt inclusions: A microscopic perspective on a complex magmatic world: Annual Review of Earth and Planetary Science, v. 49, p. 465–494, doi: 10.1146/annurev-earth-082420-060506.

Xu, T., Liu, X., Xiong, X., and Wang, J., 2022, Sulfur dissolution capacity of highly hydrated and fluid-saturated dacitic magmas at the lower crust and implications for porphyry deposit formation: Geochimica et Cosmochimica Acta, v. 333, p. 107–123, doi: 10.1016/j.gca.2022.07.004.

Zajacz, Z., Candela, P.A., Piccoli, P.M., and Sanchez-Valle, C., 2012, The partitioning of sulfur and chlorine between andesite melts and magmatic volatiles and the exchange coefficients of major cations: Geochimica et Cosmochimica Acta, v. 89, p. 81–101, doi: 10.1016/j.gca.2012.04.039.

Zhang, D., and Audétat, A., 2017, What caused the formation of the giant Bingham Canyon porphyry Cu-Mo-Au deposit? Insights from melt inclusions and magmatic sulfides: Economic Geology, v. 112, p. 221–244, doi: 10.2113/econgeo.112.2.221.

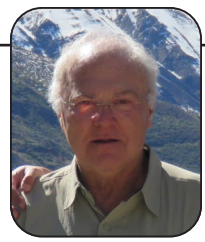

Robert Loucks completed his Ph.D. in 1984 at Harvard University. While on the faculty of Purdue University (1984–1992), he investigated the petrology of lower-crustal ultramafic-mafic cumulate complexes in Kohistan (N. Pakistan), which provided formative insights into petrogenesis of copper ore-forming arc magmas. At the Research School of Earth Sciences (RSES), Australian National University (1992–2003), he pioneered development of the world's first ArF excimer laser ablation-inductively coupled plasma-mass spectrometry system for analysis of minerals and fluid inclusions. At RSES and subsequently at the Centre for Exploration Targeting, University of Western Australia, research by Loucks and students has focused on arc magmatism related to copper and gold ore genesis.